Kinetic Features of Alpha Particles in a Pestchek-like Magnetic Reconnection Event in the Solar Wind Observed by Solar Orbiter

Die Duan[1] , Jiansen He[1] , Xingyu Zhu[1] , Rui Zhuo[1] , Ziqi Wu[1] , Georgios Nicolaou[2] , Jia Huang[3] ,
Daniel Verscharen[2] , Liu Yang[4] , Christopher J. Owen[2] , Andrey Fedorov[5] , Philippe Louarn[5], and Timothy S. Horbury[6]

[1] School of Earth and Space Sciences, Peking University, No. 5 Yiheyuan Road, Haidian District Beijing, 100871, People's Republic of China; jshept@pku.edu.cn
[2] Mullard Space Science Laboratory, University College London, Holmbury St. Mary, Dorking, Surrey, RH5 6NT, UK
[3] Space Sciences Laboratory, University of California, Berkeley, CA 94720, USA
[4] Institut für Experimentelle und Angewandte Physik, Christian-Albrechts-Universität zu Kiel, Kiel, Germany
[5] Institut de Recherche en Astrophysique et Planétologie, 9, Avenue du Colonel Roche, BP 4346, F-31028 Toulouse Cedex 4, France
[6] Space and Atmospheric Physics, The Blackett Laboratory, Imperial College London, London, SW7 2AZ, UK

Abstract

The acceleration and heating of solar wind particles by magnetic reconnection are important mechanisms in space physics. Although alpha particles (^{4}He^{2+}) are the second most abundant population of solar wind ions, their kinetic behavior in solar wind magnetic reconnection is not well understood. Using the high-energy (1500–3000 eV) range of the Solar Wind Analyser/Proton–Alpha Sensor instrument on board Solar Orbiter, we study the kinetic features of alpha particles in an exhaust region of a Pestchek-like solar-wind reconnection event with a weak guide field. A pair of back-to-back compound discontinuities is observed in the exhaust region. We find that the plasma in the magnetic exhaust region is heated and bounded by slow shocks (SSs), while the accelerated reconnection jet is bounded by rotational discontinuities (RDs). The SSs are outside the RDs, which is not expected from the magnetohydrodynamical prediction. We suggest this different location of the discontinuities is due to the enhanced parallel temperature $T_{p\parallel} > T_{p\perp}$, which reduces the local Alfvén speed in the exhaust region, allowing the SSs to propagate faster than the RDs. Inside the exhaust region, the guide field is dominant. We find a two-population distribution of the alpha particles. These two populations are field aligned downstream the SSs and shift to have a perpendicular offset in the reconnection jet, suggesting that the change of the magnetic field at the RDs has similar timescales with the proton gyroperiod, but faster than those of the alpha particles, such that the alpha particles behave like pickup ions.

Unified Astronomy Thesaurus concepts: Solar wind (1534); Solar magnetic reconnection (1504); Heliosphere (711)

1. Introduction

The solar wind is a supersonic plasma flow originating from the upper solar atmosphere. Protons are the most abundant population of solar wind ions (∼95% in terms of number density, typically $1 \sim 10$ cm^{-3} at 1 au), and alpha particles (helium-4 nuclei ^{4}He^{2+}, typically ∼0.1 cm^{-3} at 1 au) are the second most abundant population (Verscharen et al. 2019; Mostafavi et al. 2022). The ratio of the alpha particle number density to that of the protons in the solar wind is 1%∼5% and correlates with solar activity (Kasper et al. 2007). Due to its low density, the solar wind plasma is mostly collisionless, so the different species can exhibit nonequilibrium features such as different velocities and temperatures. During the evolution of the solar wind, the ions are accelerated and heated significantly (Marsch 2006; Verscharen et al. 2019). In situ measurements in the inner heliosphere and at 1 au show that heavy ions exhibit greater temperatures than the protons, suggesting a preferential heating of alpha particles and heavier ions in the solar wind (Tracy et al. 2016; Kasper et al. 2017; Kasper & Klein 2019). This process begins in the solar corona (Cranmer & Winebarger 2019) and continues into the interplanetary space. The alpha particles are often found to flow faster than the protons with the drift velocity $v_{\alpha p} = |v_\alpha - v_p|$ between $0.5v_A$ and v_A in the fast and in the Alfvénic slow solar wind, where v_s is the bulk velocity of the species s (p for protons and α for alpha particles), and $v_A = B/\sqrt{\mu_0 m_p n_p}$ is the Alfvén speed. In contrast, $v_{\alpha p}$ is close to 0 in the non-Alfvénic slow solar wind (Ďurovcová et al. 2017; Stansby et al. 2020). The velocity distribution functions (VDFs) of solar wind protons in intervals with strong Alfvénic turbulence can usually be approximated by the sum of two parts: a dominant core part and a drifting beam part. The proton core is often observed with $T_{p\perp} > T_{p\parallel}$, where $T_\perp$ and $T_\parallel$ are the temperatures in the directions perpendicular and parallel to the magnetic field direction. In contrast to the protons, alpha particles often exhibit the opposite thermal anisotropy with $T_{\alpha\parallel} > T_{\alpha\perp}$ (Marsch et al. 1982; Wilson et al. 2018; Stansby et al. 2019). The origins of the multiple anisotropic populations are still under debate. To explain the preferential heating of the different species, various processes have been suggested, including magnetic reconnection, wave–particle interactions, and turbulent stochastic heating (Drake et al. 2009; Isenberg & Vasquez 2009; Chandran et al. 2013; Kasper et al. 2013). On the other hand, the free energy in the nonequilibrium VDFs with drift velocity and/or anisotropic temperatures can lead to the growth of certain instabilities, and these unstable modes reshape the VDFs through nonlinear effects (Verscharen et al. 2013a, 2013b).

Magnetic reconnection is a prevalent physical phenomenon in space (Hesse & Cassak 2020; Lu et al. 2022). During magnetic reconnection, the magnetic field topology is changed and electromagnetic energy is converted into kinetic and thermal energies of the plasma particles. Reconnection plays a potentially very important role for the evolution of the solar wind, since it can supply energy for the acceleration and heating of the solar wind (Viall & Borovsky 2020), and facilitate the formation of mesoscale structures like "switchbacks" (Drake et al. 2021; He et al. 2021). In interplanetary space, magnetic reconnection is identified in in situ observations. Reconnection events have been observed in various solar wind environments, e.g., interplanetary coronal mass ejections, heliospheric current sheets, switchbacks, or solar wind current sheets from turbulence (Gosling et al. 2005a; Phan et al. 2006, 2021; Gosling 2007; Mistry et al. 2017; Froment et al. 2021; Owen et al. 2021). These studies report structures and kinetic features expected in a magnetic reconnection exhaust region (Gosling 2012). The transitions from the background solar wind to the exhaust region are slow-mode-like, close to the prediction of the Pestchek model with slow shocks (SSs; Gosling 2007; Feng et al. 2017). An accelerated plasma jet is observed in the magnetic reconnection exhaust region, mainly occurring within a bifurcated current sheet. The jet is bounded by two rotational discontinuities (RDs) propagating at approximately the Alfvén speed and showing plasma velocity and magnetic field variations conforming to the Walén relation. The plasma density and temperature are enhanced inside the exhaust region (Mistry et al. 2017). Magnetic reconnection can heat the plasma directly and produce multiple energetic ion populations (Lavraud et al. 2021; Phan et al. 2022). The increase in proton temperature can be caused not only by the dissipation of the reconnecting current sheet but also by the mutual mixing from the two sides outside the jet flow region. In this way, the pair of back-to-back RDs generate a pattern of counterstreaming velocity distributions with a relative drift speed of approximately twice the Alfvén speed (Gosling et al. 2005b; He et al. 2018). Such a VDF with counterstreaming, field-aligned particle populations can become firehose-unstable and excite additional Alfvénic fluctuations, thus enhancing the turbulence level in the jet flow region (He et al. 2018). In solar wind observations and magnetohydrodynamic (MHD) simulations, the RDs are always found upstream the SSs and bound the exhaust region, while another type of structure with external SSs and internal RDs is found in some particle-in-cell (PIC) simulations with guide field (Innocenti et al. 2017), when the PIC simulation domain extends long enough downstream the exhaust region to allow for the development of SSs and RDs (Liu et al. 2012).

Previous observations of the VDFs of ions have mainly focused on the protons, while the way in which alpha particles are affected by solar wind magnetic reconnection is still unclear. Drake et al. (2009) suggest that heavy ions can be heated by a pickup mechanism as $\Delta T_i = 1/3 m_i v_{\rm jet}^2$ in the exhaust region with weak guide fields, where ΔT_i is the ion temperature increment in the exhaust region, m_i is the ion mass, and $v_{\rm jet}$ is the speed of the reconnection jet. A statistical study by Drake et al. (2009) finds that ΔT_p is smaller than predicted, while alpha particles are heated 4 times more than the protons, in agreement with the prediction. To better understand the behavior of alpha particles, we here study their kinetics using high-resolution 3D ion VDF measurements from the Solar

Orbiter mission during a solar wind reconnection event. We find that magnetic reconnection can produce multiple populations of alpha particles. The instruments and methods used in the work are introduced in Section 2, and the observations are presented in Section 3. We summarize our result and discuss the implications in Section 4.

2. Instrumentation and Method

Solar Orbiter (SolO) was launched on 2020 February 10, carrying a variety of instruments for in situ solar wind observation and remote sensing of the solar atmosphere (Müller et al. 2020). The local magnetic field B is measured by the Solar Orbiter MAGnetometer (MAG) at 8 Hz (Horbury et al. 2020), and the Solar Wind Analyser (SWA) suite provides the measurement of solar wind particles (Owen et al. 2020). SWA measures both protons (p) and alpha (α) particles with the Proton–Alpha Sensor (SWA/PAS) at 0.25 Hz. The bulk properties of the ions, such as their density n_i, bulk velocity V_i, and temperature T_i, are calculated on ground as the moments of 3D VDFs f_i. The Electron Analyser System (SWA/EAS) measures the 3D VDFs of electrons at a cadence of 10 s or 100 s. We calculate the pitch-angle distribution of the suprathermal electrons between 70 and 163 eV to diagnose the magnetic connectivity to the Sun.

PAS measures the VDFs $f_i(E, \theta, \phi)$ of proton and alpha particles simultaneously, where E, θ, and ϕ are the energy bin, elevation angle, and azimuthal angle of PAS, respectively. We extract the proton and alpha particles individually from the measured ion VDF, $f_i(E, \theta, \phi)$, via the following process:

(i) We convert $f_i(E, \theta, \phi)$ from the PAS instrument frame to a magnetic-field-aligned frame $f_i(v_\parallel, v_{\perp 1}, v_{\perp 2})$, where $v_\parallel$ is along the direction of B (averaged over the sampling time of PAS), and $v_{\perp 1,2}$ are orthogonal to $v_\parallel$.

(ii) The mass-to-charge ratio of alpha particles is twice that of the protons, so an alpha particle has twice the energy per charge of a proton with the same velocity. To separate the two populations, we determine the energy per charge E_m, with the lowest omnidirectional energy flux of ions between 800 eV q^{-1} and 1400 eV q^{-1}, and treat all measurements with $E < E_m$ as protons f_p, and all measurements with $E > E_m$ as alpha particles f_α, where E is the energy per charge of the individual measurement bins and q is the charge of the particle under consideration. Then, we integrate f_p and f_α individually to calculate the bulk parameters (moments) of f_p and f_α. This method is similar to the method used by Marsch et al. (1982). It potentially underestimates the density and temperature of alpha particles and overestimates their bulk velocity if a nonnegligible number of alpha particles have energy per charge lower than E_m. We use the synthetic data method suggested by Scudder (2015) to construct artificial VDFs of protons and alpha particles and to estimate the error of the truncated-moment method. The error in the proton moments using this method is very small, while the error in the alpha particle moments strongly depends on the temperature of the protons and of the alpha particles. In the cold inflow regions, this error is negligible. In the hot exhaust regions, the truncated-moment method underestimates the alpha particle temperature by about 20%–30%, while the errors in density and velocity are relatively small.

To analyze the structure of the exhaust region, we adopt the Walén analysis to identify RDs (He et al. 2018) and the Rankine–Hugoniot shock-fitting method to calculate the shock
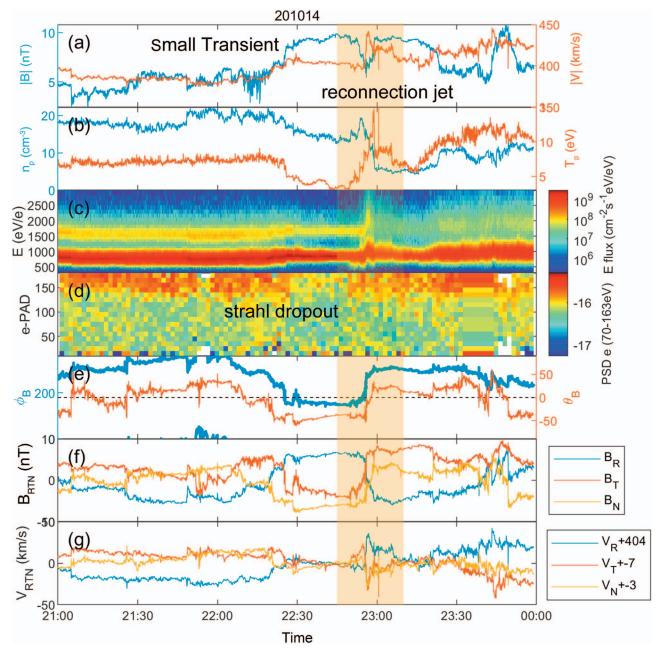
Figure 1. Time series plots of a crossing of a small transient event on 2020 October 14. (a) Magnetic field and solar wind speed. (b) Proton density and temperature. (c) Differential energy flux of protons and alpha particles. (d) Pitch-angle distribution of superthermal electrons (70–163 eV). (e) The azimuth ϕ_B and elevation angle θ_B of the magnetic field. (f)–(g) Magnetic field components and solar wind velocity in RTN coordinates. The yellow-shaded region is the magnetic reconnection event, which is detailed in Figure 2.

parameters and identify SSs (Koval & Szabo 2008). To confirm the shock is a SS, we calculate the slow Mach number $M_s = V_n/c_{sl}$, where V_n is the bulk velocity in the shock frame in the shock normal direction, and c_{sl} is the local phase speed of slow magnetosonic waves. SSs must have $M_s > 1$ upstream the shock and $M_s < 1$ downstream.

3. Observation and Analysis

On 2020 October 14, SolO passed through a small transient event in the solar wind. On this date, SolO was located at 0.99 au away from the Sun and 126° away from the Sun–Earth line.

Figure 1 displays the measurement overview of the crossing. The magnetic field and the ion bulk velocity are presented in the radial-tangential-normal (RTN) coordinate system. SolO is immersed in the slow solar wind with $V_{SW} < 450$ km s^{-1}. The suprathermal strahl electrons are centered at a pitch angle of 180°. Together with the anti-sunward magnetic field, this orientation indicates that the solar wind is magnetically connected to the Sun. SolO crosses a structure with a smooth rotation (22:00–22:30 UT) of the magnetic field and a dropout (22:30–22:50 UT) of the strahl electrons. The enhancement of the magnetic field and the decrease of the ion density and temperature without a bipolar magnetic field are similar to the features of the small transient events described by Kilpua et al. (2009). At the boundary (around 22:50–23:00 UT), SolO observes a clear reconnection jet with a reversal of the radial magnetic field and a decrease of the magnetic field.
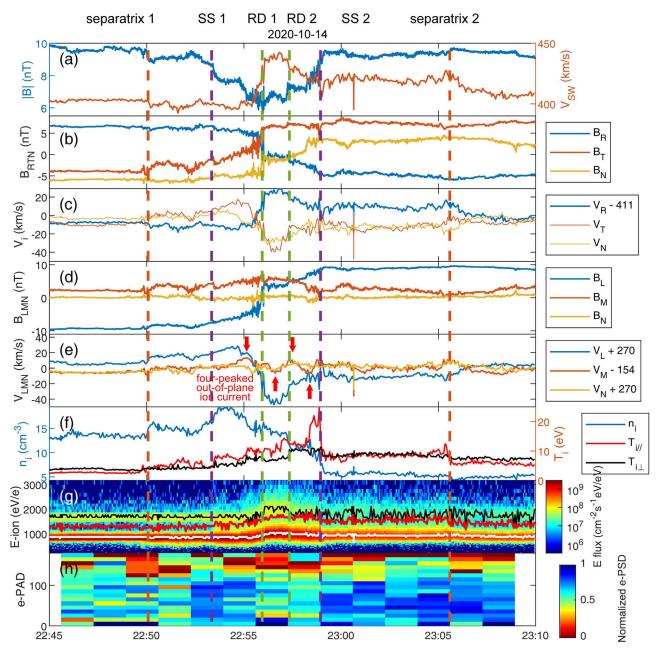
Figure 2. Overview of the reconnection event. (a) Magnetic field and solar wind speed. (b)–(c) Magnetic field and proton bulk velocity in RTN coordinates. (d)–(e) Magnetic field and proton bulk velocity in LMN coordinates. (f) Proton density, parallel and perpendicular temperature. (g) Differential energy flux of protons and alpha particles. The white line marks the energy with maximum proton flux, and the black line marks the energy with maximum alpha particle flux; the red line marks the energy per charge E_m with minimum flux between the distributions of protons and alpha particles. (h) Pitch-angle distribution of suprathermal electrons (70–163 eV). The green dashed lines mark the two rotational discontinuities, the purple dashed lines mark the two slow shocks, and red dashed lines mark the separatrices of the reconnection exhaust region.

The parameters of the reconnection exhaust region are shown in more detail in Figure 2. SolO crosses the exhaust region (bounded by the purple dashed lines) from the high-density ($n_i \approx 12 \, \mathrm{cm}^{-3}$) to the low-density solar wind ($n_i \approx 4 \, \mathrm{cm}^{-3}$), when the radial magnetic field component B_R reverses from 6 to -6 nT and the magnetic field $|B|$ drops from 9.4 to 6.5 nT with a signature of a bifurcated current sheet. A plasma jet (bounded by green dashed lines) is observed as a rapid increase of V_{SW} to 440 km s^{-1}, accompanied by an increase of n_i, $T_{i\parallel}$, and $T_{i\perp}$. The proton plasma beta $\beta_p = n_p k_B T_p / [B^2/(2\mu_0)]$ is 0.2 on both sides of the event. The local Alfvén speed is $V_{\mathrm{A1}} \sim 60$ km s^{-1} before the entry into the

exhaust region, and $V_{\mathrm{A2}} \sim 90$ km s^{-1} after the reconnection event.

A minimum variance analysis is implemented to estimate the orientation of the current sheet, through which we transform the bulk velocity and magnetic field into the LMN frame. The N direction is the normal vector of the current sheet given by $[-0.66, -0.06, -0.75]$ in the RTN frame. The current sheet is associated with a medium guide field (out-of-plane field along the M direction) of $B_M = 5 \, \mathrm{nT} \approx 0.5 \langle |B_L| \rangle$ with a $160°$ magnetic shear angle (the L direction refers to the direction with the maximum change of the magnetic field). The reconnection jet speed is 50 km s^{-1} along the $-L$ direction
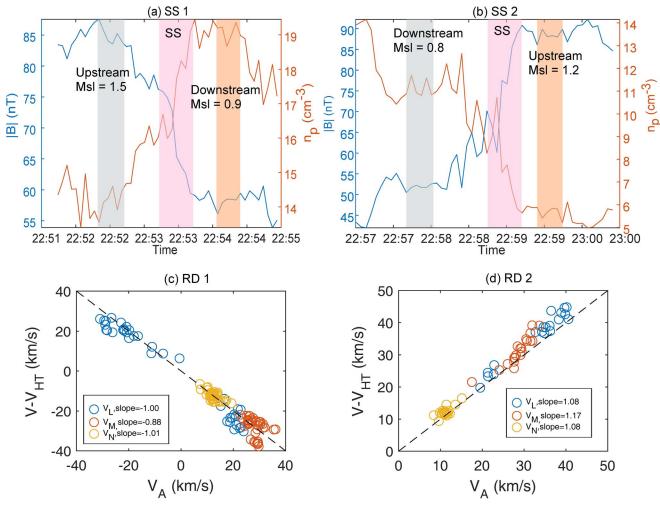
Figure 3. (a) Magnetic field (blue) and ion number density (red) across SS1. The pink square marks the shock, and the gray and orange squares mark the upstream and downstream regions of the shock used in the shock fitting. (b) Same as (a) but for SS2. (c) Walén test result for RD1. V_{HT} is the moving velocity component of the de Hoffman–Teller reference frame in the spacecraft reference frame. (d) Walén test result of RD2.

(anti-sunward), thus SolO is located anti-sunward of the X-line. The average bulk solar wind speed along the normal direction of the current sheet is $V_N = 270$ km s^{-1}, so the width of the exhaust region is approximately 81,000 km ≈ 1000 d_i (5 minutes crossing; here, $d_i = v_A/\Omega_p$ is the proton inertial length, and $\Omega_p = eB/m_p$ is the proton gyrofrequency). The approximate opening angle of the exhaust is 4°, and the estimated distance between the reconnection X-line and SolO is 2×10^6 km (25,000 d_i), indicating that SolO is well outside the (extended) ion diffusion region.

As shown in Figure 2, the solar wind magnetic field exhibits five discontinuities across the exhaust region, indicating the complex structure of the reconnection event. The separatrices, at which the solar wind parameters deviate from the background, are marked by red dashed lines. Outside the separatrices, the proton and alpha particles are separated well in the omnidirectional energy flux (Figure 1(g)). When SolO travels through the separatrices, the density and temperature increase, with $T_{i\parallel}$ exceeding $T_{i\perp}$. We find a pair of SSs (marked by purple lines) and a pair of RDs inside the SSs (marked by green lines) in the exhaust region. The exhaust region is bounded by the SS pair, and the reconnection jet is bounded by the RD pair.

Figure 3 shows the results of our shock-fitting and Walén analysis. These results are consistent with the features of RDs and SSs. The shock speed is 361 km s^{-1} for SS1 and 208 km s^{-1} for SS2 in the spacecraft frame. The shock normal direction is $(-0.20, -0.11, 0.97)$ for SS1 and $(-0.38, -0.86, 0.33)$ for SS2 in LMN coordinates. Both SSs are quasi-perpendicular shocks as predicted by the Petschek model. The angle between the magnetic field and the shock normal direction θ_{Bn} is 75° upstream SS1, 70° downstream SS1, 50° downstream SS2, and 60° upstream SS2. This SS/RD compound structure is similar to the simulations of Innocenti et al. (2017). In addition, the out-of-plane ion velocity V_M shows a four-peaked pattern downstream the SSs, which is also consistent with these simulations.

The bulk properties of the protons (calculated from fitting) and of the alpha particles (calculated from integration of the truncated VDF) are shown in Figure 4. The alpha particle density n_α is close to 0.1 cm^{-3} before the entry, and 0.05 cm^{-3} upon exit. The ratio $n_\alpha/n_p \approx 0.008$ in the transient event is smaller than in the background solar wind where $n_\alpha/n_p \approx 0.01$. The drift velocity $v_{\alpha p} = |v_p - v_\alpha|$ is close to 0 in the ambient solar wind, and both proton and alpha particles are accelerated to the same speed in the exhaust region by $\Delta V_L \approx 45$ km s^{-1}. The heating of the particles is very asymmetric. Both T_p and T_α
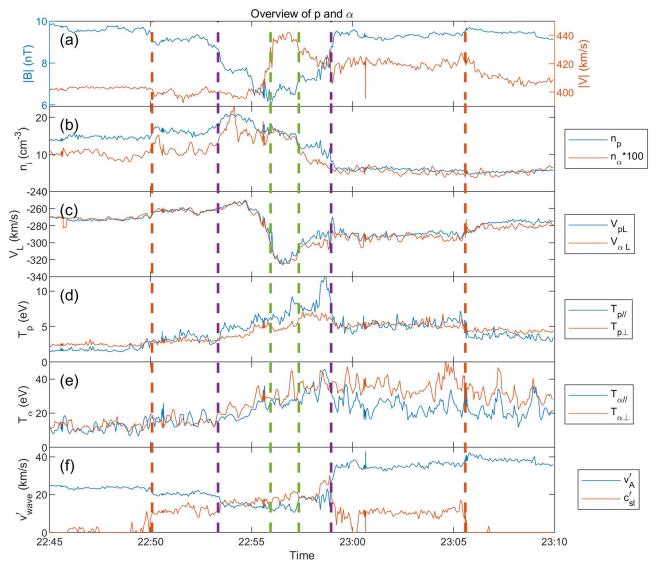
Figure 4. Parameters of protons and alpha particles during the reconnection event. (a) Magnetic field and solar wind speed. (b) Number densities of protons n_p (blue) and alpha particles $n_\alpha \times 100$ (red). (c) Bulk velocity components of protons (blue) and alpha particles (red) along the L direction in LMN coordinates. (d) Parallel (blue) and perpendicular (red) temperatures of the protons. (e) Same as (d) but for the alpha particles. (f) Modified Alfvén wave speed v'_A (blue) and slow wave speed c'_{sl} (red) calculated with the temperature anisotropy for $\theta = 65°$. The vertical dashed lines are the same as in Figure 2.

are significantly enhanced inside the exhaust region, but the downstream region of SS2 has the highest temperature. $T_{p\parallel}$ increases from 1.7 to 5.3 eV downstream of SS1, and reaches 10.1 eV downstream of SS2. We find $T_{p\parallel} < T_{p\perp}$ outside the exhaust and $T_{p\parallel} > T_{p\perp}$ inside the exhaust. In contrast with the protons, the alpha particles have higher $T_{\alpha\perp} > T_{\alpha\parallel}$ inside the exhaust region. $T_{\alpha\perp}$ increases from 10 to 35 eV, and $T_{\alpha\parallel}$ increases from 10 to 30 eV downstream SS2. To estimate the ion heating, we calculate the average temperature in the exhaust region $T_{i,\text{exhaust}}$, and calculate the effective inflow temperatures $T_{i,\text{inflow,eff}}$ as

$$T_{i,\text{inflow,eff}} = \frac{n_{i1} T_{i1}/B_{L1} + n_{i2} T_{i2}/B_{L2}}{n_{i1}/B_{L1} + n_{i2}/B_{L2}}, \qquad (1)$$

which is the weighted average of ion temperatures on both inflow sides indicated by subscripts 1 and 2, with the weight being the ratio of the number density to the magnetic field along the L direction (Phan et al. 2014). The effective inflow temperature is defined as the ratio of the total inflow thermal energy flux

to the total inflow particle flux, which reads $k_B T_{\text{inflow,eff}} = k_B(n_1 T_1 V_{\text{inflow,1}} + n_2 T_2 V_{\text{inflow,2}})/(n_1 V_{\text{inflow,1}} + n_2 V_{\text{inflow,2}})$; here, V_{inflow} is the inflow speed. Assuming the electric fields E_{inflow} are equal on the two inflow sides according to the steady-state assumption and estimating them as $E_{\text{inflow}} = B_{L1}V_{\text{inflow,1}} = B_{L2}V_{\text{inflow,2}}$, we obtain Equation (1). We find $T_{p,\text{inflow,eff}} = 2.7$ eV and $T_{\alpha,\text{inflow,eff}} = 15.2$ eV for the inflow, and $T_{p,\text{exhaust}} = 5.4$ eV and $T_{\alpha,\text{exhaust}} = 27.1$ eV for the exhaust region. Therefore, the average increase in the temperatures is $\Delta T_p = 2.7$ eV and $\Delta T_\alpha = 11.9$ eV. We find that the alpha particle heating is approximately 4 times stronger than the proton heating, in particular $\Delta T_i = 0.14 m_i \Delta V_{i,L}^2$, which is close to the observation by Drake et al. (2009) of $\Delta T_i = 0.13 m_i \Delta V_{i,L}^2$.

In MHD theory, SSs propagate at a speed of c_{sl}, which is always less than the propagation speed of RDs at v_A. However, a temperature anisotropy can decrease the local Alfvén speed. According to Abraham-Shrauner (1967), the modified Alfvén speed v'_A and slow magnetosonic speed c'_{sl} for an anisotropic
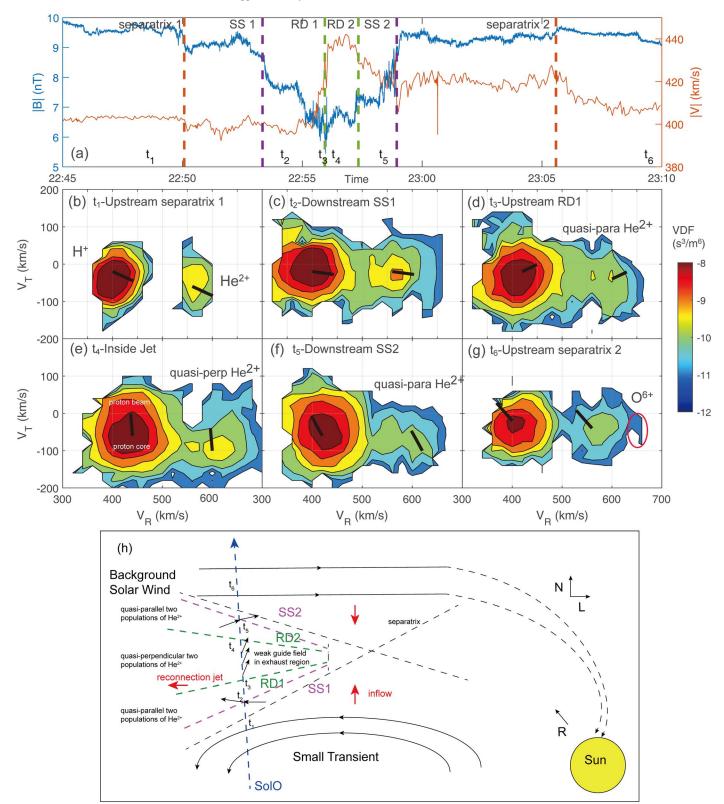
Figure 5. (a) Magnetic field (blue) and solar wind speed (red). The vertical dashed lines are the same as in Figure 2. (b)–(g) 2D cuts of the ion VDF in the *R*–*T* plane at the time stamps as indicated in panel (a). The black lines indicate the magnetic field direction. The length of the black line is the local Alfvén speed in the *R*–*T* plane. The starting points of the black lines represent the maximum values of the VDF for both protons and alpha particles. (h) Illustration of this reconnection event in the *L*–*N* plane. Black arrows show the direction of the magnetic field. The red arrows represent the direction of the plasma bulk velocity. The purple dashed lines show the position of the SSs, and the green dashed lines represent the RDs. The blue dashed arrow represents the trajectory of Solar Orbiter.

plasma can be expressed as

$$v'_A/v_A = \sqrt{\frac{\beta_\perp}{2} - \frac{\beta_\parallel}{2} + 1} \cos\theta, \qquad (2)$$

$$c'_{sl}/v_A = \sqrt{A - \frac{1}{2}\sqrt{B^2 + C}}, \qquad (3)$$

where the coefficients A, B, and C are

$$A = \frac{1}{2}\left[1 + \beta_\perp\left(1 - \frac{1}{2}\cos^2\theta\right) + \beta_\parallel\cos^2\theta\right], \qquad (4)$$

$$B = 1 + \beta_\perp(1 - \cos^2\theta) - 2\beta_\parallel\cos^2\theta, \qquad (5)$$

$$C = 2\beta_\perp^2 \sin^2\theta\cos^2\theta. \qquad (6)$$

Here, θ is the angle between the magnetic field and the wavevector. Figure 4(f) shows the modified wave speeds for $\theta = 65°$ (the average θ_{Bn} downstream the two SSs). The enhanced temperature anisotropy leads to $c'_{sl} > v'_A$ in the exhaust region, which allows the SSs to propagate faster and thus be located outside the RDs.

A selection of VDFs measured by PAS are shown in Figure 5 (2D cut on the R–T plane). Since the velocity of the coordinates is calculated as $v = \sqrt{2q_p U/m_p}$, where U represents the voltage of the energy bin of the PAS and $q_p = e$ represents the proton electric charge; the velocity value of the alpha particles shown in Figure 5 is $\sqrt{2}$ times their actual velocity $v_\alpha = \sqrt{2q_\alpha U/m_\alpha} = v/\sqrt{2}$ ($q_\alpha = 2q_p$, $m_\alpha = 4m_p$). In panels (b) and (g) outside the exhaust region, protons and alpha particles have such low temperatures that their VDFs separate well. Downstream SS1 before the reversion of the magnetic field, the proton and alpha particles are mainly heated in parallel direction (panels (c)–(d)). An antiparallel alpha particle beam occurs between the peaks of the protons and the alpha particles. In panel (d), the alpha particles have a pattern of two populations parallel to the local magnetic field direction with similar intensity. Downstream SS2, the alpha particles also exhibit two populations, as shown in panel (f), but the density is much smaller than in panel (d). Inside the reconnection jet (panel (e)), both protons and alpha particles are accelerated, exhibiting beam signatures along the magnetic field direction. Moreover, the alpha particles have two populations distributed perpendicular to the local magnetic field. This pattern is also observed in Figure 2 of Lavraud et al. (2021). The drift velocity between the two alpha particle populations is close to the local Alfvén speed (37 km s^{-1} in the exhaust region), which is much smaller than the sum of the two upstream Alfvén speeds (60 km s^{-1} + 90 km s^{-1} = 150 km s^{-1}). Therefore, the two populations do not originate from the penetrating upstream alpha particles (Gosling et al. 2005a), but are more likely to be produced by magnetic reconnection itself. Test-particle simulations by Drake et al. (2009) show that the bouncing movement of ions between the boundaries of the exhaust region can generate two populations along the perpendicular direction, which is consistent with our observation. Previous observations and simulations find that multiple proton populations can be generated in reconnection events, and we report that magnetic reconnection can produce multiple populations of alpha particles as well. The timescale of magnetic field change at the RDs is approximately 2 s, matching the proton gyrofrequency $\Omega_p = 0.6$ Hz. The field changes faster than the alpha particle gyrofrequency of $\Omega_\alpha = 0.3$ Hz, making the alpha particles behave like pickup ions.

4. Discussion and Conclusions

We report a magnetic reconnection event between the magnetic fields of a small transient structure and the ambient solar wind in SolO observations. Our interpretation of the geometry of the event is illustrated in Figure 5(h). The reconnection exhaust region is Pestchek-like with a pair of compound boundaries composed of external SSs and internal RDs. Both proton and alpha particles are heated inside the exhaust region. We report for the first time that the alpha particles exhibit multiple populations in the reconnection exhaust. We identify populations with similar densities but different bulk velocities parallel to the magnetic field downstream the SSs in the exhaust region. The two populations shift to a perpendicular offset in the reconnection jet region. The behavior of the alpha particles indicates that they experience a pickup heating process.

Owen et al. (2021) describe a multilayer structure of exhaust regions in the solar wind depending on the magnetic field and plasma conditions. Our observation confirms such a multilayer structure and suggests a new scenario with external SSs and internal RDs. However, our work only focuses on the magnetic field and the plasma ions. The electron behavior in the complex exhaust region needs measurements with higher time resolution.

PIC simulations predict a four-peaked out-of-plane ion current pattern, multiple ion populations, and increased $T_\parallel/T_\perp$ downstream the SSs (Innocenti et al. 2017), which is consistent with our observations. However, protons and alpha particles behave differently in the observations. The alpha particles exhibit multiple populations with changing profiles inside the exhaust, while the protons experience strong core heating without counterstreaming beams. A possible explanation for this behavior is that both protons and alpha particles consist of multiple populations, but we cannot see the proton beam since it possibly overlaps with the alpha particles in energy-per-charge space. The proton beams can only be observed when the magnetic field deviates from the radial direction because the alpha particles distribute around higher v_R regions than protons in the field of view of PAS.

Inside the exhaust region, the free energy associated with the multiple ion populations generated by magnetic reconnection allows instabilities to grow as seen in the observation that the fluctuations of the magnetic field are enhanced near RD1 and SS2 in Figure 2(b). The temperature anisotropy and the existence of the proton and alpha particle beams can trigger different kinds of instabilities, such as the firehose instability, the Alfvén/ion-cyclotron instability, and the fast-magnetosonic/whistler instability (Verscharen et al. 2013a; He et al. 2018; Liu et al. 2019). To develop a complete picture of the structure and energy conversion of magnetic reconnection, identifying wave modes and analyzing the mechanisms of wave generation will be needed.

We observe an additional particle population located at around $V_R = 650$ km s^{-1} in Figure 5(g). This population might be O^{6+}, whose mass-to-charge ratio is $8/3$ (if we assume the bulk velocity of O^{6+} is equal to the protons, the oxygen ions would be located at around 400 km s$^{-1} \times \sqrt{8/3} \approx 650$ km s^{-1}). This additional population potentially leads to a slight overestimation of the density,

radial velocity, and temperature of the alpha particles in our analysis. The kinetic behavior of other heavy ions in magnetic reconnection needs further observations and simulations in the future.

ORCID iDs

Die Duan https://orcid.org/0000-0002-6300-6800
Jiansen He https://orcid.org/0000-0001-8179-417X
Xingyu Zhu https://orcid.org/0000-0002-1541-6397
Rui Zhuo https://orcid.org/0000-0003-4726-9755
Ziqi Wu https://orcid.org/0000-0002-1349-8720
Georgios Nicolaou https://orcid.org/0000-0003-3623-4928
Jia Huang https://orcid.org/0000-0002-9954-4707
Daniel Verscharen https://orcid.org/0000-0002-0497-1096
Liu Yang https://orcid.org/0000-0002-6416-1538
Christopher J. Owen https://orcid.org/0000-0002-5982-4667
Andrey Fedorov https://orcid.org/0000-0002-9975-0148
Timothy S. Horbury https://orcid.org/0000-0002-7572-4690

References

Abraham-Shrauner, B. 1967, JPlPh, 1, 361
Chandran, B. D. G., Verscharen, D., Quataert, E., et al. 2013, ApJ, 776, 45
Cranmer, S. R., & Winebarger, A. R. 2019, ARA&A, 57, 157
Drake, J. F., Agapitov, O., Swisdak, M., et al. 2021, A&A, 650, A2
Drake, J. F., Swisdak, M., Phan, T. D., et al. 2009, JGRA, 114, A05111
Ďurovcová, T., Šafránková, J., Němeček, Z., & Richardson, J. D. 2017, ApJ, 850, 164
Feng, H., Li, Q., Wang, J., & Zhao, G. 2017, SoPh, 292, 53
Froment, C., Krasnoselskikh, V., Dudok de Wit, T., et al. 2021, A&A, 650, A5
Gosling, J. T. 2007, ApJL, 671, L73
Gosling, J. T. 2012, SSRv, 172, 187
Gosling, J. T., Skoug, R. M., McComas, D. J., & Smith, C. W. 2005a, JGRA, 110, A01107
Gosling, J. T., Skoug, R. M., McComas, D. J., & Smith, C. W. 2005b, GeoRL, 32, L05105
He, J., Zhu, X., Chen, Y., et al. 2018, ApJ, 856, 148
He, J., Zhu, X., Yang, L., et al. 2021, ApJL, 913, L14
Hesse, M., & Cassak, P. A. 2020, JGRA, 125, e25935
Horbury, T. S., O'Brien, H., Carrasco Blazquez, I., et al. 2020, A&A, 642, A9
Innocenti, M. E., Cazzola, E., Mistry, R., et al. 2017, GeoRL, 44, 3447
Isenberg, P. A., & Vasquez, B. J. 2009, ApJ, 696, 591
Kasper, J. C., & Klein, K. G. 2019, ApJL, 877, L35
Kasper, J. C., Klein, K. G., Weber, T., et al. 2017, ApJ, 849, 126
Kasper, J. C., Maruca, B. A., Stevens, M. L., & Zaslavsky, A. 2013, PhRvL, 110, 091102
Kasper, J. C., Stevens, M. L., Lazarus, A. J., Steinberg, J. T., & Ogilvie, K. W. 2007, ApJ, 660, 901
Kilpua, E. K. J., Luhmann, J. G., Gosling, J., et al. 2009, SoPh, 256, 327
Koval, A., & Szabo, A. 2008, JGRA, 113, A10110
Lavraud, B., Kieokaew, R., Fargette, N., et al. 2021, A&A, 656, A37
Liu, Y.-H., Drake, J. F., & Swisdak, M. 2012, PhPl, 19, 022110
Liu, Z., Zhao, J., Sun, H., et al. 2019, ApJ, 874, 128
Lu, Q., Fu, H., Wang, R., & Lu, S. 2022, ChPhB, 31, 089401
Marsch, E. 2006, LRSP, 3, 1
Marsch, E., Rosenbauer, H., Schwenn, R., Muehlhaeuser, K. H., & Neubauer, F. M. 1982, JGR, 87, 35
Mistry, R., Eastwood, J. P., Phan, T. D., & Hietala, H. 2017, JGRA, 122, 5895
Mostafavi, P., Allen, R. C., McManus, M. D., et al. 2022, ApJL, 926, L38
Müller, D., St. Cyr, O. C., Zouganelis, I., et al. 2020, A&A, 642, A1
Owen, C. J., Bruno, R., Livi, S., et al. 2020, A&A, 642, A16
Owen, C. J., Foster, A. C., Bruno, R., et al. 2021, A&A, 656, L8
Phan, T. D., Drake, J. F., Shay, M. A., et al. 2014, GeoRL, 41, 7002
Phan, T. D., Gosling, J. T., Davis, M. S., et al. 2006, Natur, 439, 175
Phan, T. D., Lavraud, B., Halekas, J. S., et al. 2021, A&A, 650, A13
Phan, T. D., Verniero, J. L., Larson, D., et al. 2022, GeoRL, 49, e96986
Scudder, J. D. 2015, ApJ, 809, 126
Stansby, D., Matteini, L., Horbury, T. S., et al. 2020, MNRAS, 492, 39
Stansby, D., Perrone, D., Matteini, L., Horbury, T. S., & Salem, C. S. 2019, A&A, 623, L2
Tracy, P. J., Kasper, J. C., Raines, J. M., et al. 2016, PhRvL, 116, 255101
Verscharen, D., Bourouaine, S., & Chandran, B. D. G. 2013a, ApJ, 773, 163
Verscharen, D., Bourouaine, S., Chandran, B. D. G., & Maruca, B. A. 2013b, ApJ, 773, 8
Verscharen, D., Klein, K. G., & Maruca, B. A. 2019, LRSP, 16, 5
Viall, N. M., & Borovsky, J. E. 2020, JGRA, 125, e26005
Wilson, L. B. I., Stevens, M. L., Kasper, J. C., et al. 2018, ApJS, 236, 41